NRC·CNRC

NRC Publications Archive
Archives des publications du CNRC

High-speed imaging and statistics of puffing and micro-exploding droplets in spray-flame synthesis

Jüngst, N.; Skenderović, I.; Südholt, B. A.; Smallwood, G. J.; Kruis, F. E.; Kaiser, S. A.

This publication could be one of several versions: author's original, accepted manuscript or the publisher's version. / La version de cette publication peut être l'une des suivantes : la version prépublication de l'auteur, la version acceptée du manuscrit ou la version de l'éditeur.
For the publisher's version, please access the DOI link below./ Pour consulter la version de l'éditeur, utilisez le lien DOI ci-dessous.

Publisher's version / Version de l'éditeur:
https://doi.org/10.1016/j.jaecs.2023.100167
Applications in Energy and Combustion Science, 15, C, 2023-01-24

NRC Publications Archive Record / Notice des Archives des publications du CNRC :
https://nrc-publications.canada.ca/eng/view/object/?id=6bcde085-7694-452b-887e-bc8b22375cbe
https://publications-cnrc.canada.ca/fra/voir/objet/?id=6bcde085-7694-452b-887e-bc8b22375cbe

Access and use of this website and the material on it are subject to the Terms and Conditions set forth at
https://nrc-publications.canada.ca/eng/copyright
READ THESE TERMS AND CONDITIONS CAREFULLY BEFORE USING THIS WEBSITE.

L'accès à ce site Web et l'utilisation de son contenu sont assujettis aux conditions présentées dans le site
https://publications-cnrc.canada.ca/fra/droits
LISEZ CES CONDITIONS ATTENTIVEMENT AVANT D'UTILISER CE SITE WEB.

Questions? Contact the NRC Publications Archive team at PublicationsArchive-ArchivesPublications@nrc-cnrc.gc.ca. If you wish to email the authors directly, please see the first page of the publication for their contact information.

Vous avez des questions? Nous pouvons vous aider. Pour communiquer directement avec un auteur, consultez la première page de la revue dans laquelle son article a été publié afin de trouver ses coordonnées. Si vous n'arrivez pas à les repérer, communiquez avec nous à PublicationsArchive-ArchivesPublications@nrc-cnrc.gc.ca.

National Research Council Canada   Conseil national de recherches Canada

Canada

Applications in Energy and Combustion Science 15 (2023) 100167

Contents lists available at ScienceDirect

Applications in Energy and Combustion Science

journal homepage: www.sciencedirect.com/journal/applications-in-energy-and-combustion-science

High-speed imaging and statistics of puffing and micro-exploding droplets in spray-flame synthesis

N. Jüngst [a,c,*], I. Skenderović [b,c], B.A. Südholt [a,c], G.J. Smallwood [d], F.E. Kruis [b,c], S.A. Kaiser [a,c]

[a] Institute for Energy and Materials Processes – Reactive Fluids University of Duisburg-Essen, Duisburg, Germany
[b] Institute of Technology for Nanostructures, University of Duisburg-Essen, Duisburg, Germany
[c] CENIDE, Center for Nanointegration Duisburg-Essen, University of Duisburg-Essen, Duisburg, Germany
[d] Metrology Research Centre, National Research Council Canada, Ottawa, ON, Canada

ARTICLE INFO

Keywords:
Spray-flame synthesis
Droplet puffing and micro-explosion
Microscopy
High-speed imaging
Image analysis
Population balance modelling

ABSTRACT

Thermally-induced breakup of metal-precursor-laden droplets in spray-flame synthesis occurs via a rapid and disruptive disintegration, i.e., “puffing” and “micro-explosion”. To assess the temporal evolution and statistics of droplet disruption, LED-illuminated droplet shadowgraphs were imaged with a microscope onto a high-speed camera and morphological image analysis was applied. The atomized liquid was a mixture of 35 vol.-% ethanol and 65 vol.-% 2-ethylhexanoic acid mixed with iron(III) nitrate nonahydrate (INN) as a precursor. Droplet evaporation and disruption were also simulated with a population balance model. The model finds solid precipitates forming in the droplets because of the decomposition of the precursor intermediate iron(III) 2-ethylhexanoate. The precipitates form a particle shell, which favors the superheating of the droplets' interior, and they facilitate heterogeneous bubble nucleation. Imaging experiments and modelling find that per 10 μs lifetime of a droplet, the probability for disruption increases from 5 to 13% and 5 to 19%, respectively, when increasing the INN concentration from 0.05 to 0.5 mole/l. The probability of disruption suggests that throughout their lifetime in the spray flame, nearly all droplets will undergo disruption and many of them multiple times. In the experiment, droplets before disruption are 15% smaller than regular, non-disrupting droplets. Once disrupted, the droplets have a 45% smaller mean diameter than regular droplets. Under all conditions, disrupting and disrupted droplets are slower than regular droplets while the disruption does not significantly accelerate disrupted droplets.

1. Introduction

Spray-flame synthesis (SFS) uses inexpensive and low-volatile precursors for the generation of functional nanomaterials, required for catalysis, batteries, and sensors [1–3]. Thus, the technique is advantageous over classical gas-phase synthesis which requires pre-vaporizing the precursors fed into the process [4]. However, to produce small and homogeneous metal-oxide nanoparticles, a rapid and complete evaporation of the precursor-laden droplets is desired in SFS (gas-to-particle route). Experiments on single combusting precursor-laden droplets show a disruptive non-aerodynamic, i.e., at very low Weber number, breakup of the droplets [5–7]. This thermally-induced breakup, in the following termed droplet disruption, is further classified into puffing (weak disruption [8] with local surface rupture of the droplet and ejection of a single secondary droplet) and micro-explosion (the violent disintegration of large parts of the droplet into multiple fragments) [9]. Droplet disruption is thought to be beneficial for rapid spray evaporation and considered a key step in SFS. Precursor solutions showing disruption in SFS were found to produce single-phase particle with a high specific-surface area and narrow size distribution, in contrast to non-disrupting solutions [10,11].

Most studies on disrupting droplets investigate single combusting droplets of fuel/water-emulsions [12–22] or binary fuel mixtures, being in solution or with limited miscibility [23–28], where the components have significantly different boiling points. Models predicting the time until droplet breakup as well as critical temperatures were developed based on experiments of single combusting multicomponent (two--component or emulsified) droplets [29,30]. Schlieren and extinction measurements were done to investigate the sooting tendency of such disrupting droplets [31]. Fig. 1 summarizes schematically the thermally-induced breakup of multicomponent droplets. The heat

---

* Corresponding author at: Institute for Energy and Materials Processes – Reactive Fluids University of Duisburg-Essen, Duisburg, Germany.
E-mail address: niklas.juengst@uni-due.de (N. Jüngst).

https://doi.org/10.1016/j.jaecs.2023.100167
Received 28 March 2023; Received in revised form 7 June 2023; Accepted 22 June 2023

Abbreviation

E	Erupted droplet
EHA	2-ethylhexanoic acid
EtOH	Ethanol
F	Fragments
Fe-eh	Iron(III) 2-ethylhexanoate
FOV	Field of view
fps	Frames per second
HAB	Height above burner
INN	Iron(III) nitrate nonahydrate
M	Mole/liter
PDI	Phase doppler interferometry
R	Regular/deformed droplet
SFS	Spray-flame synthesis
slm	Standard liter per minute

Symbols

A	area (m^2)
Ar	Arrhenius number (-)
b	Breakage function (-)
c	Droplet concentration ($\#/m^3$)
d	Area-equivalent diameter (m)
d_{FOV}	Depth of the measurement volume (m)
E	Evaporation rate (m^3/s)
h_{FOV}	Height of the measurement volume (m)
h_{group}	Vertical length of a feature group (m)
I	Raw spray image (counts)
I_0	Bright field image – without spray (counts)
I^*	Bright-field corrected spray image (-)
J	Nucleation rate ($\#/(m^3 \bullet s)$)
k	Decomposition rate (1/s)
k_0	Kinetic prefactor (1/s)
l	Projected distance in the x-y-plane (m)
N	Total number of in-focus features (-)
n_D	Number concentration of droplets ($\#/m^3$)
n_{Fe-eh}	Number concentration of Fe-eh molecules ($\#/m^3$)
$n_{Fe(OH)_3}$	Number concentration of monomers ($\#/m^3$)
n_P	Number concentration of particles ($\#/m^3$)
S^*	Fragmentation rate (1/s)
t	Time (s)
t_{LED}	Time between two LED pulses (s)
T	Temperature (K)
T_{decomp}	Decomposition temperature (K)
v	Volume (m^3)
v_P	Volume of parent droplet (m^3)
v^*	Critical droplet volume (m^3)
v'	Volume of larger particle (m^3)
$\bar{v}_d$	Average droplet velocity (m/s)
w_{FOV}	Width of the measurement volume (m)
x, y	Coordinates of bounding boxes (m)
β	Collision rate constant (m^3/s)
φ	Particle volume-fraction (-)
φ^*	Critical particle volume-fraction (-)
σ_{v_d}	Standard deviation in the droplet velocity (m/s)

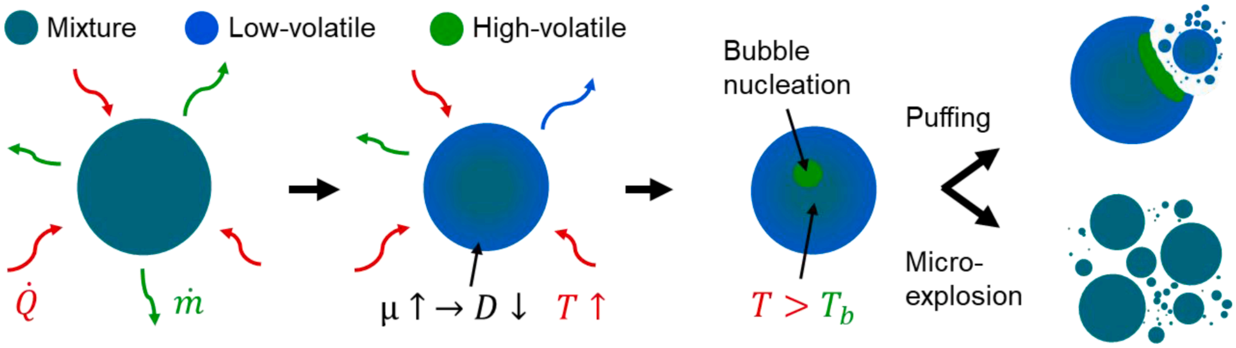

Fig. 1. Thermally-induced droplet breakup.

transferred from the flame to the droplet causes a rapid and preferential evaporation of the high-volatile component from the surface, while the interior of the droplet conserves the initial composition. Thus, the high-viscous and low-volatile droplet surface can superheat the droplet interior where it comes to bubble nucleation and growth, followed by droplet puffing (locally) or micro-explosion [27,32].

Only few studies document the direct visualization of droplet disruption in spray flames [33–38]. For direct visualization of droplet disruption, typically, in both single-droplet and spray-flame experiments, droplet shadowgraphs are imaged onto a high-speed camera. In our previous work and that of Stodt et al., disruption of precursor-laden droplets was observed in SFS [39,40].

In SFS of iron oxide nanoparticles, the precursor iron(III) nitrate nonahydrate (INN) is typically dissolved in a mixture of ethanol (EtOH) and 2-ethylhexanoic acid (EHA). In the presence of dissolved iron ions (Fe^{3+}), the solvent rapidly reacts to water and 2-ethylhexanoate (eh) while the latter then reacts to the complex iron(III) 2-ethylhexanoate (Fe-eh) [41]. Even though vapor-liquid equilibrium measurements of EtOH/EHA solutions show strong preferential evaporation of EtOH [42], we have shown that droplet disruptions in SFS do not occur for the solvent only but when INN is added to the solvent [40]. Our preliminary results show that also sprays of EtOH + INN, and that is consistent with single-droplet experiments [43,44], and emulsions of water + EtOH/EHA do not show droplet disruption. From that, we conclude that droplet disruption cannot only be caused by superheating of EtOH or water. Instead, disruption might be linked to precursor chemistry and products of thermal decomposition of Fe-eh.

For high molecular-weight precursors such as hexanoates and acetylacetonates, decomposition temperature and species composition strongly depend on sample geometry [45]. In experiments on the creation of metal-oxide films, metallic-precursor films with a thickness below 1 µm were heated via the irradiance of near-infrared light. A thin film of liquid Fe-eh fully decomposes at 375 K forming solid FeO_x and Fe as well as gaseous products [46,47]. However, thermogravimetric analysis of Fe-eh in a 'bulk' finds full decomposition and solid α-Fe_2O_3 formation at only 537 K. This is because the thin film has a higher

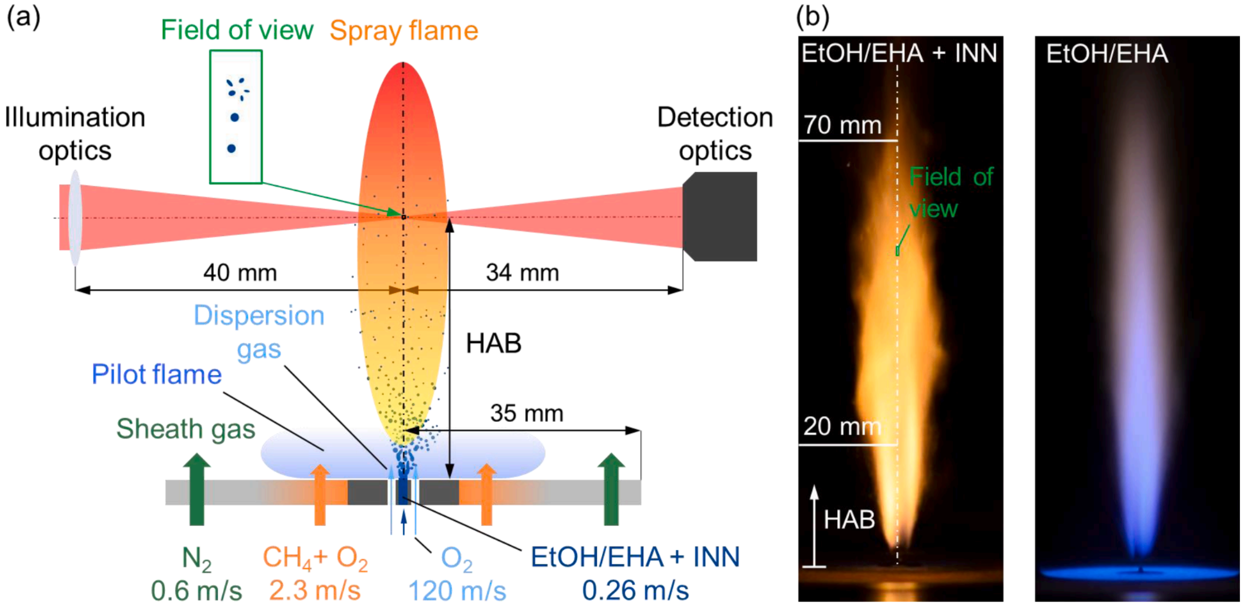

Fig. 2. (a) Sketch of SpraySyn burner, optics, and probe volume. (b) Photographs of the spray flame's luminosity.

surface-area-to-volume-ratio which increases outwards diffusion of gaseous decomposition products and thus accelerates the decomposition reaction. Regarding spray droplets, the thin-film case is more applicable as precursor species tend to accumulate at the droplet surface as a thin layer. Thus, in the solvent EtOH/EHA (boiling temperature about 450 K) solids are likely to precipitate, as already observed as large and edgy particles in the product (droplet-to-particle) [48]. The precipitates then also make the particle shell more viscous and act as nuclei during heterogeneous bubble nucleation.

Metal or metal-oxide particles suspended in a combustible liquid, 'nanofuels', were already found to cause disruption when ignited [49–54]. Depending on the particle loading, a combusting droplet will disrupt differently. While at light loading the droplet undergoes a continuous ejection of small droplets and gas (related to puffing), at high loading the droplet disrupts more catastrophically (micro-explosion). The latter case is most likely related to a viscous particle shell that surrounds the droplet, traps a forming bubble, and thus hinders the mass transport of fuel through the surface. In contrast, at light loadings shell formation is avoided by continuous bubble nucleation at nanoparticles at the droplet surface and subsequent ejection of bubbles and droplets [55]. In combusting droplets of jet fuel, dispersed with boron nanoparticles, the onset of micro-explosion became earlier with increasing particle loading [56]. In precursor-laden single droplets, the onset of micro-explosion also became earlier when nanoparticles were suspended [5]. The motion of large particle aggregates within the droplets was even observed with shadowgraphy [57].

In our previous experimental work, we developed high-speed high-magnification shadowgraphy to visualize droplet disruption in SFS of iron oxide nanoparticles [40]. There, we saw direct evidence of droplet disruption in the flame and that this only happened if the precursor was present. Now that we know this is a frequent and important process, the next step is to quantify the process' probability, which is almost entirely unknown in the spray flame, as well as sizes, velocities, and concentrations of the participating droplets as a function of precursor concentration and position in the flame. An existing image analysis scheme was extended for evaluating these quantities. Probabilities and droplet sizes are compared with those from a population balance model of droplets and particles, the latter precipitating in the droplets. Some model parameters were derived from single-droplet experiments of the same material system, as reported in detail in the companion paper to this one [58].

2. Methods

2.1. Spray-flame burner

A standardized spray-flame burner, named "SpraySyn", is used in this work for nanoparticle synthesis, schematically shown in Fig. 2a [2, 40]. A syringe pump feeds the precursor/solvent mixture at 2 ml/min (nominal exit velocity 0.26 m/s) through a capillary in the center of the burner matrix. The solvent is EtOH/EHA. For nanoparticle synthesis, variable amounts of INN are added to the solvent, yielding concentrations of 0.05 – 0.5 mole/l (M) INN in EtOH/EHA. Oxygen flows at 120 m/s (10 slm) through a concentric gap, atomizing the liquid. A lean premixed methane/oxygen flame ($\dot{V}_{CH_4} = 2$ slm and $\dot{V}_{O_2} = 16$ slm, exit velocity 2.3 m/s) concentrically surrounds the atomization zone and forms a flat pilot flame that stabilizes the spray flame. A nitrogen co-flow at 0.6 m/s (120 slm) shields the entire process from the environment. Under these operating conditions, flame instabilities in the SpraySyn burner cause the spray flame being pulsating with approximately 667 Hz and 50% of the time extinguished [59]. Fig. 2b shows photographs of the flame luminosity of two spray flames burning EtOH/EHA + 0.2 M INN and EtOH/EHA only. Also indicated are the approximate size of the field of view (FOV) at about 50 mm HAB and the downstream range (20 to 70 mm HAB) in which measurements were performed. In this burner configuration, Stodt et al. found Weber numbers of 0.006 – 0.03 between 20 to 70 mm HAB. Those Weber numbers are much below the critical Weber number of about 1 such that aerodynamic disintegration is very unlikely in these regions of the spray flame [60].

The atomization of the liquid results in small and fast droplets. Phase Doppler Interferometry (PDI) measurements indicate droplet diameters and velocities of 22.5 µm and 91 m/s, respectively, at 40 mm HAB [59]. Therefore, imaging the droplets requires both high resolution in space (high magnification) and time (short illumination). At the same time, the FOV needs to cover sufficient streamwise distance to capture the spatio-temporal evolution of a droplet disruption. This tradeoff is addressed in the following section.

2.2. High-speed, high-magnification shadowgraphy

Details on the illumination and the detection are given in our previous work [40]. In this work, the LED pulse duration was reduced from 200 to 100 ns by using a commercial laser-diode driver (Picolas LDP-V

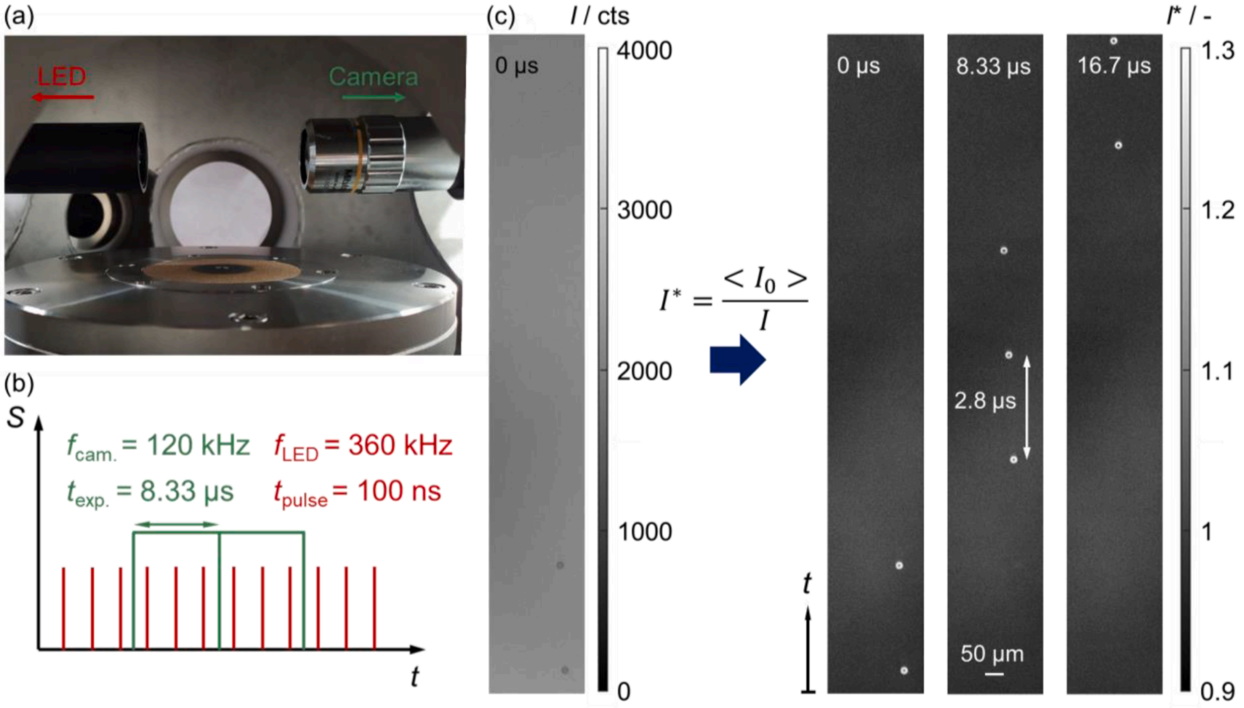

Fig. 3. (a) Optical layout in reactor, (b) imaging strategy: Three LED pulses in single camera frame exposure, (c) image processing: Dividing single raw image by bright field image (without spray) yields color inversion in corrected images. Each image shows up to three consecutive shadowgraphs due to stacking three LED pulses.

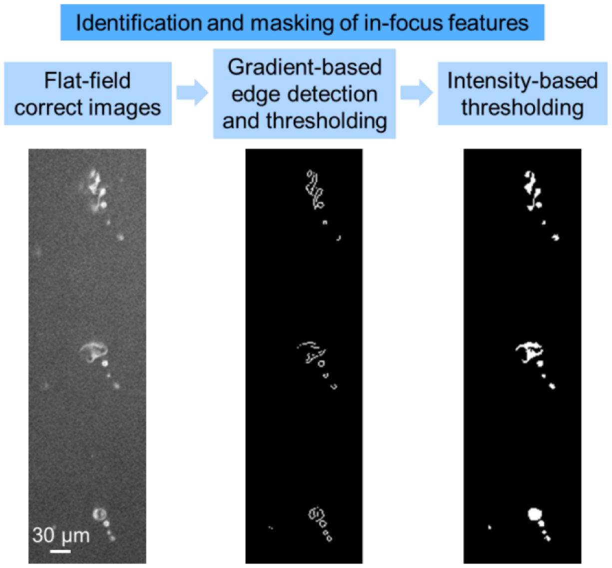

Fig. 4. Photometric processing and gradient- and intensity-based thresholding to identify in-focus features and estimate morphological metrics, as shown in more detail in [40].

50-100 V3.3) instead of our previously used homebuilt driver [40]. This provides less blurring, higher gradient and contrast in the imaged shadowgraphs. Köhler-type illumination enabled high light collection efficiency from the LED and a localized and homogeneous illumination of the FOV at the same time. On the detection side, a microscope (microscope objective: Mitutoyo M Plan APO 10x) was used to image droplet shadowgraphs onto the sensor of a high-speed camera (Photron Fastcam SA-Z). This yields a magnification of 11.1 and a projected pixel size in the object plane of 1.8 µm/pixel. The camera sensor was cropped to 1024 • 144 pixels which results in a FOV of 1.8 mm height and 0.26 mm width. Considering an average droplet velocity of 80 m/s (as at 50 mm HAB), the length of the FOV images a droplet's shadowgraph for about 22.5 µs.

Fig. 3a shows a photograph of the optical layout above the SpraySyn burner within the reactor. The acquisition time diagram of the LED with respect to the camera is shown in Fig. 3b. The camera was operated at a repetition rate of 120 000 frames/second (fps). Within each frame's exposure an LED burst of three pulses was triggered at a frequency of 360 000 fps. This approach results in a continuous sequence of temporally equally spaced droplet shadowgraphs among the images. Stacking three shadowgraphs on a single image was found to yield reasonable temporal resolution while maintaining sufficient contrast for automatic image analysis.

Fig. 3c shows a raw image containing three droplet shadowgraphs as well as a processed version of this and temporally subsequent images. Image processing follows a division of the ensemble averaged bright field images I_0 – images without spray – by the raw spray images I, yielding the processed image I^*. Note that both I and I_0 are dark (background) corrected. In the processed images, the shadowgraphs now appear brighter than the background (color inverted). Measurements were done at 20, 30, 40, 50, 60, and 70 mm HAB. At each HAB, the INN concentration in the solvent was varied between 0.05, 0.1, 0.2, 0.3, 0.4, and 0.5 M, yielding a total of 36 measurements. All measurements were done on the centerline of the spray flame and the ones at 50 mm HAB and those at 0.2 M INN were done three times to assess their repeatability. For a robust statistical analysis of the frequencies of regular, disrupting, and disrupted droplets, 150 000 images were acquired (total acquisition time of 1.25 s) in each measurement. Considering the spray flame's pulsation frequency of 667 Hz, a single measurement includes approximately 833 flame-on and flame-off periods. The large data set requires an automatic image analysis scheme for extracting event frequencies, droplet sizes, velocities, and concentrations. This is described in the following section. Due to the high droplet concentration there, at 20 mm HAB frequencies of puffing and micro-explosion were manually evaluated via visual inspection of 10 000 images.

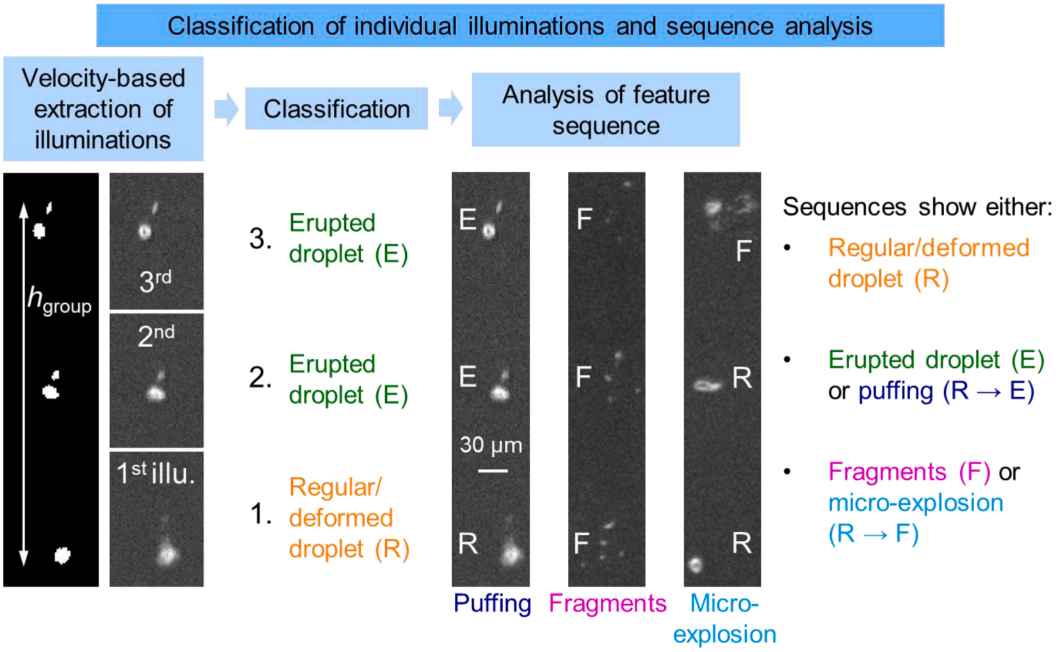

Fig. 5. Extraction and classification of each illumination and analysis of consecutive illuminations. Discrimination of sequences showing regular, disrupting (puffing or micro-exploding), and disrupted (erupted droplets or fragments) droplets.

2.3. *Image analysis*

In our previous work [40], we presented an image analysis scheme for finding in-focus droplets/features and their morphological metrics. The flow chart in Fig. 4 summarizes this. First, a Sobel operator finds sharp edges in the flat-field corrected images (Fig. 3c). This determines the magnitude of the intensity gradient in every pixel. Then, thresholding the intensity-gradient image at a value of 0.0325 yields a binarized image, with bright pixels indicating feature/droplet contours.

As discussed in [40], a constant threshold biases the in-focus features towards larger droplets. Thus, a custom-made microscope slide (JD Photo Data) with opaque circular dots, ranging from 2–40 μm in diameter, was positioned at different distances from the focal plane via a translation stage. In the images of the slide, the number of edge pixels for every dot size was determined as a function of the distance from the focal plane (results not shown here). With this information a size-dependent minimum number of edge pixels can be determined for each diameter. This relation also finds that features within +/- 42.5 μm from the focal plane are "in-focus", while features further away are discarded. Uncertainty from the translation stage's micrometer screw might result in an inaccuracy of 2.4% in the calculated probe volume and the resulting droplet concentration.

Further processing (not shown here) fills the features' contours and labels all individual in-focus features within an image. Within the smallest rectangle enclosing each feature, Otsu's [61] intensity-based thresholding is applied to the flat-field corrected images I^*. From the binarized image, the area A and the area-equivalent diameter d can be calculated:

$$d = \sqrt{\frac{4\,A}{\pi}} \tag{1}$$

Therefore, the smallest detected droplet size corresponds to a single pixel, yielding d = 2 μm. However, it is possible that smaller droplets are detected but that their size is then assigned to a single pixel. Droplet concentrations were calculated by first counting all in-focus features in a measurement. The sum is then divided by the measurement volume. The measurement volume results from the product of the size of the FOV, the depth of the FOV (85 μm), a factor correcting for the flow downstream, and the number of images in a measurement. Details are given in appendix A1.

Fig. 5 on the left shows that features with small horizontal distance and certain vertical distance, h_{group}, are very likely to stem from one, two, or three illuminations and are considered a group. In our previous work, regular/non-disrupting and disrupting droplets (there comprising disrupting and disrupted droplets) were distinguished by considering the number of features within a group, their distances, and their circularities. In this work, we improved the discrimination by assigning each feature to an illumination within a group, as shown in the velocity-based extraction of illuminations in Fig. 5. Based on h_{group}, the average droplet velocity at the corresponding HAB, its standard deviation, and the time between two LED pulses, the group is divided into as many equally high boxes as illuminations are found. Details on the procedure are given in the appendix A2.

In a next step, features within each illumination box are classified as described in the following. If a single feature is found, the illumination shows a regular or deformed droplet (abbreviated as "R"), but as a single entity. If exactly two features are found, the illumination shows an erupted droplet (abbreviated as "E"), as a result of a puffing event. If more than two features are found, the illumination shows fragments (abbreviated as "F") as a result of a micro-explosion. Then the temporal sequence of illuminations is analyzed. Note, that a sequence may even consist of multiple groups and thus expand over multiple images. A sequence shows either a regular, disrupting or already disrupted droplet. Disruption events are characterized by initially showing a regular droplet (among the first illuminations) which then erupts and leaves behind an erupted droplet (puffing event) or micro-explodes and leaves behind fragments. Already disrupted droplets show either erupted droplets or fragments as a result of puffing or micro-explosion, respectively, which happened further upstream. Fig. 5 on the right shows example sequences and summarizes the possible sequences.

The results of the automatic image segmentation were judged against visual inspection of the images. The inspection was done for several hundred images for each class. We found that 97, 94, 95, 96, and 95% of the sequences tagged as regular droplet, erupted droplet, fragments, puffing, and micro-explosion, respectively, were identified correctly. Around 98% of the images containing features in-focus are identified by the algorithm.

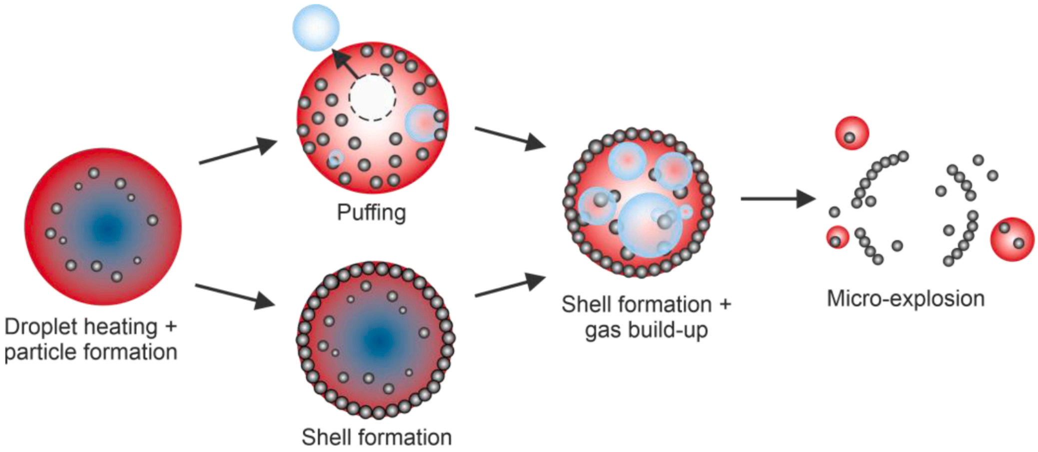

Fig. 6. Sketch of droplet disruption mechanisms as used for modelling. Only in case of micro-explosion new droplets are generated.

2.4. Population balance modelling

Population balance equations of droplets and particles, forming as precipitates within droplets, are solved. The temporal evolution of the droplet size distribution is governed by evaporation and fragmentation. The population balance equation for droplets of volume v is defined as:

$$\frac{\mathrm{d}n_\mathrm{D}(v)}{\mathrm{d}t} = -\frac{\partial[E(v)n_\mathrm{D}(v)]}{\partial v} - \delta(v^* - v)\frac{\partial[E(v)n_\mathrm{D}(v)]}{\partial v}\bigg|_{v=v^*} - S^*(v)n_\mathrm{D}(v) + \int_v^\infty S^*(v_\mathrm{P})b(v, v_\mathrm{P})n_\mathrm{D}v_\mathrm{P}\mathrm{d}v \tag{2}$$

The first two terms on the right side describe the droplets' size change due to evaporation with the rate $E(v)$. If droplets shrink to the volume v^* (corresponds to a droplet with a diameter of 2 µm), they are removed from the simulation as denoted by the Dirac-delta function. The third and fourth term describe droplet concentration decrease by fragmentation at a rate S^* and concentration increase due to explosion of larger droplets, respectively. The rate S^* is calculated at every time-step of the simulation, while the breakage function $b(v, v_\mathrm{P})$ is obtained from imaging using the volume of the parent droplet v_P, see [58].

With respect to heat-and mass transfer within the liquid phase, EtOH, EHA, water, and Fe-eh are chosen as components. Heat and mass transfer are assumed to be spherically symmetric and diffusion-limited. The combustion model and equations are same as in [62], including equal binary mass diffusion coefficients for all components. Further details regarding the implementation of the combustion model, including a comparison of the results with single droplet experiments, are given in [58].

The particle population is obtained by solving the population balance equation for particles of volume v at the droplet core and surface:

$$\frac{\mathrm{d}n_\mathrm{P}(v)}{\mathrm{d}t} = \int_0^v \beta(v - v', v')n_\mathrm{P}(v - v')n_\mathrm{P}(v')\mathrm{d}v' - n_\mathrm{P}(v)\int_0^\infty \beta(v, v')n_\mathrm{P}(v')\mathrm{d}v' + J(t)\delta(v^* - v) \tag{3}$$

This population balance equation is integrated using the pivot method from [63]. The first two terms on the right-hand side define particle concentration change due to coagulation of particles with volume v and v'. Solely perikinetic collisions are considered in the droplet core, while for the surface shell perikinetic and orthokinetic collisions are considered, the latter resulting from droplet surface regression [50]. Since Brownian diffusion for agglomerates is very slow (Peclet number >> 1), orthokinetic collision is the dominant coagulation mode in the surface shell. The perikinetic collision-rate constant β is calculated using Smoluchowki's coagulation kernel for the continuum regime [64]. Hydrodynamic interactions are included as dominant inter-particle forces (steric or electric stabilization neglected) by applying the correction function from [65]. Nucleation, $J(t)$, is controlled by decomposition of Fe-eh ($2\cdot\mathrm{Fe(C_8H_{15}O_2)_3}$) and subsequent precipitation. The following simplified global reaction step, derived from cyclic voltammetry and gas chromatography [46,47], is used:

$$2\cdot\mathrm{Fe(C_8H_{15}O_2)_3(l)} + \mathrm{O_2(aq)} \rightarrow 2\cdot\mathrm{Fe^{3+}(aq)} + 3\cdot\mathrm{C_8H_{15}O_2(l)} + \mathrm{C_7H_{14}(l)} + 2\cdot\mathrm{C_7H_{14}O(l)} + 3\cdot\mathrm{CO_2(g)} \tag{4}$$

with solid-phase formation from $\mathrm{Fe^{3+}(aq)}$ according to [66]:

$$\mathrm{Fe^{3+}(aq)} + 3\cdot\mathrm{OH^-(aq)} \rightleftharpoons \mathrm{Fe(OH)_3(s)} \tag{5}$$

The production of $\mathrm{Fe(OH)_3}$-monomers is set to follow a first order reaction,

$$J(t) = \frac{\mathrm{d}n_{\mathrm{Fe(OH)_3}}}{\mathrm{d}t} = k\cdot n_{\mathrm{Fe-eh}} \text{ with } k = k_0\cdot e^{Ar\left(1 - \frac{T_\mathrm{decomp.}}{T}\right)} \tag{6}$$

with the dimensionless Arrhenius number Ar, which was set to 1. The decomposition temperature, $T_\mathrm{decomp.}$, was set to 375.15 K. The kinetic prefactor k_0 was varied between 50 and 10^{10} 1/s, and $k_0 = 550$ 1/s was used in this work, which was found from simulations of single-droplet experiments, as described in [58]. The droplet core temperature T is calculated from a volume-weighted average of the radial temperature distribution.

The decomposition products heptene ($\mathrm{C_7H_{14}}$), boiling point of 371 K, and 3-heptanone ($\mathrm{C_7H_{14}O}$), boiling point of 420 K, are likely to become superheated during droplet combustion and cause bubble nucleation in the droplet. The produced $\mathrm{CO_2}$ further contributes to gas build-up. Additionally, the solid precipitates of $\mathrm{Fe(OH)_3}$ provide nucleation sites for gas bubbles. Furthermore, particles accumulate at the surface during evaporation and thus increases the particle volume-fraction φ. At every timestep, it is checked if φ in the surface cell reached a critical value $\varphi^* = 0.1625$, from [67]. If $\varphi \geq \varphi^*$, the particle shell has formed. If the critical temperature and the critical particle volume-fraction are met, the fragmentation rate S^* becomes equal to the droplet number concentration divided by the timestep dt. Otherwise, S^* is zero.

Fig. 6 summarizes the possible disruption modes in the modelling. Here, puffing of a droplet is considered as a superheating of 3-heptanone in the droplet core resulting in a weak disruption with gas blown out of the droplet. Particles might also form a shell before the droplet superheats and that ends up in a micro-explosion. Analog to this, superheated droplets, which have already shown puffing, might form a shell within future timesteps and also end up in a micro-explosion In a micro-explosion, the droplet then bursts into multiple fragments, as documented in [58]. The fragments have the same particle concentration and

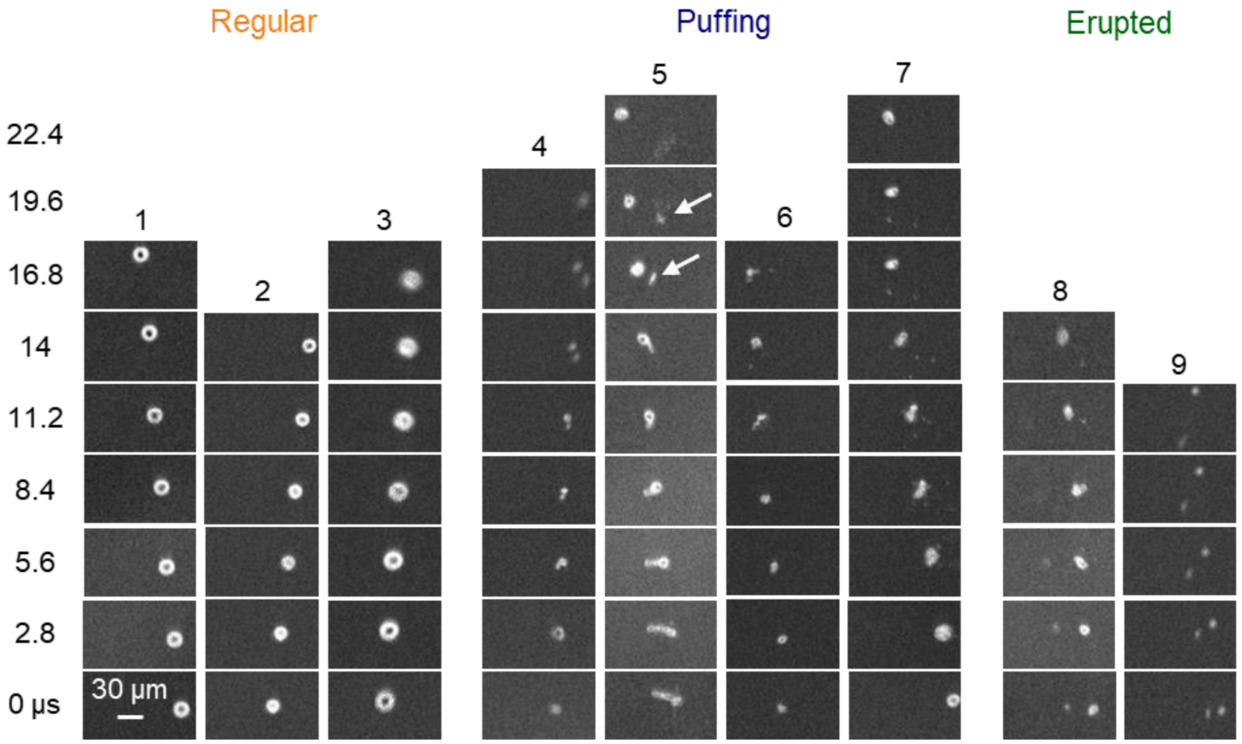

Fig. 7. Sequences of regular droplets, puffing, and erupted droplets from combusting EtOH/EHA + INN at different concentrations at 50 mm HAB.

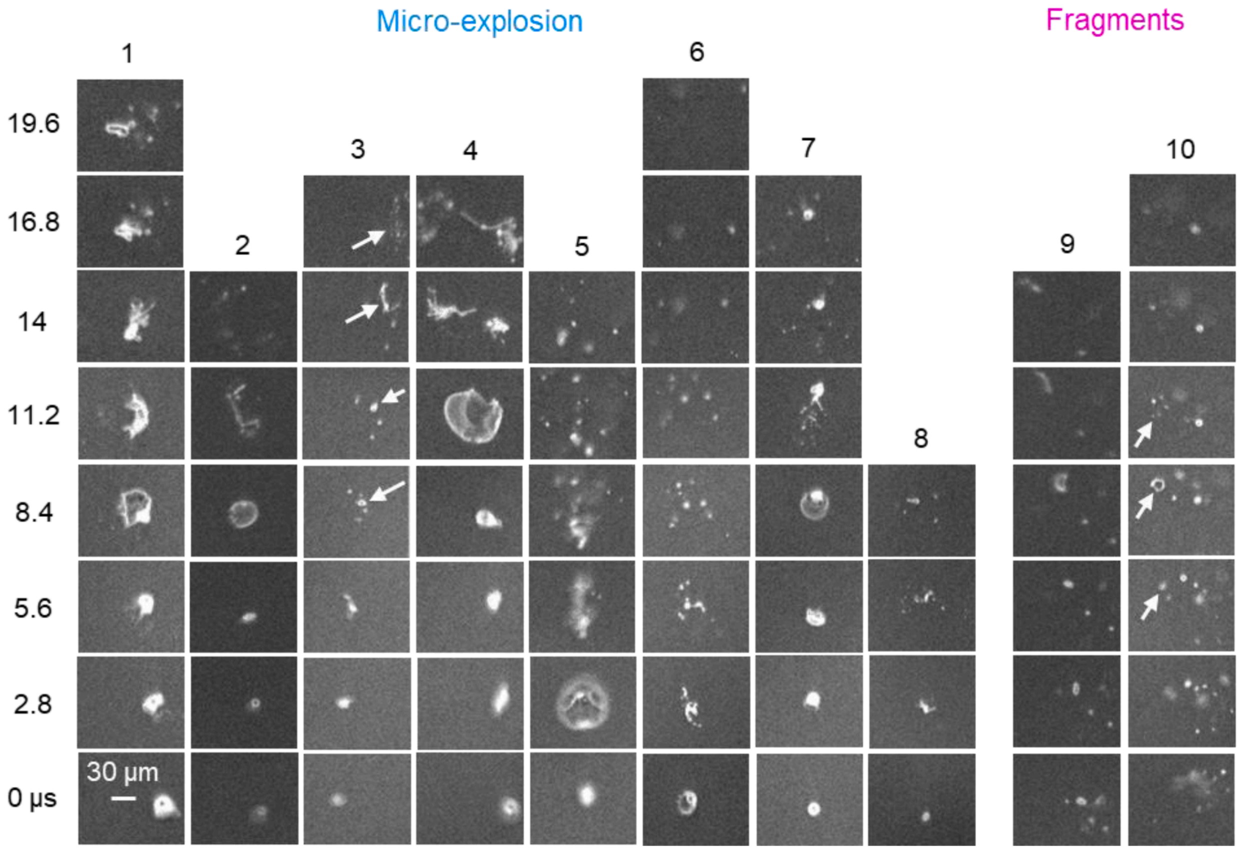

Fig. 8. Sequences of micro-explosions and fragments from combusting EtOH/EHA + INN at different concentrations at 50 mm HAB.

particle size distribution as the core of the initial droplet, i.e., just before the micro-explosion, while the shell is ejected into the gas phase.

For the population balance simulation, gas temperature and velocity were 2300 K [60] and 100 m/s [59], respectively, spatially homogeneous and constant. Simulations at 500 K gas temperature were done to account for flame-off periods. Diameters of regular droplets and

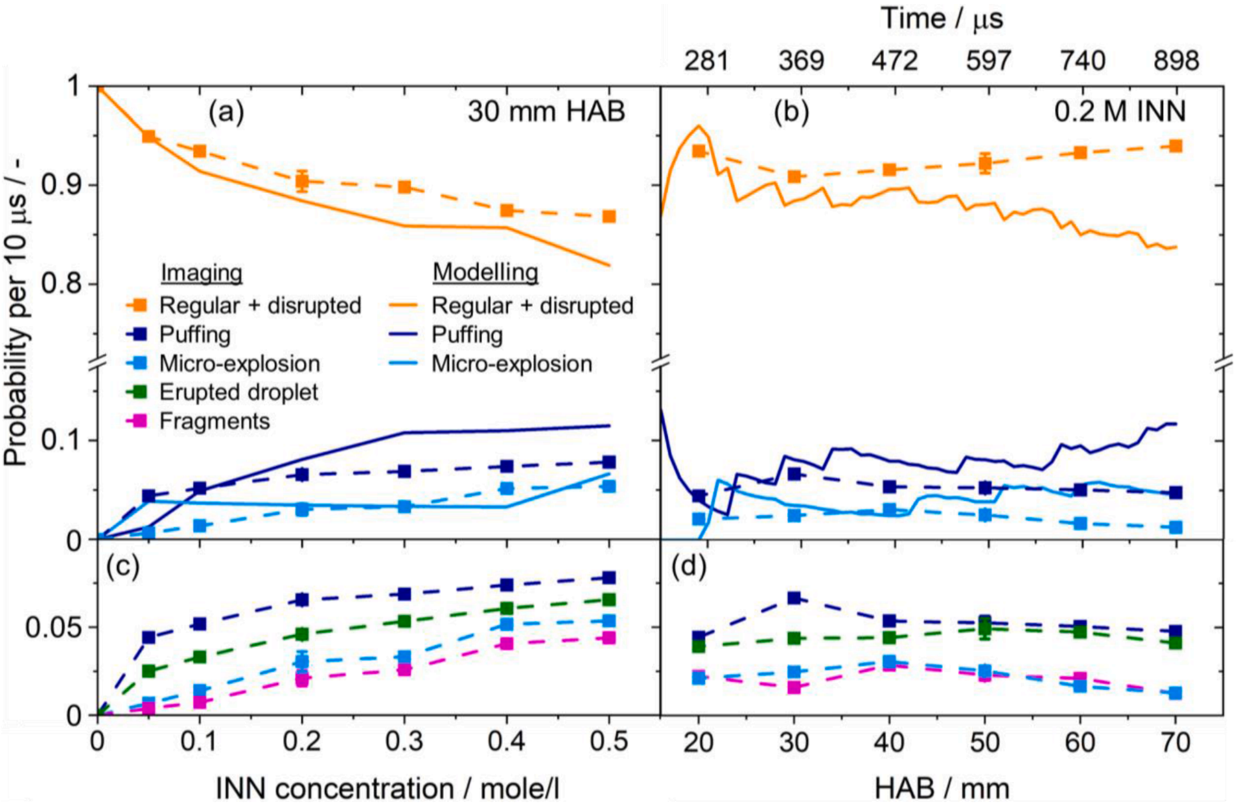

Fig. 9. Probability per 10 µs for finding regular + disrupted droplets, puffing, micro-explosion, erupted droplets, or fragments versus (a, c) the INN concentration and (b, d) the HAB. Error bars at 0.2 M INN and 50 mm HAB indicate the standard deviation among three individual measurements, each comprising 150.000 images.

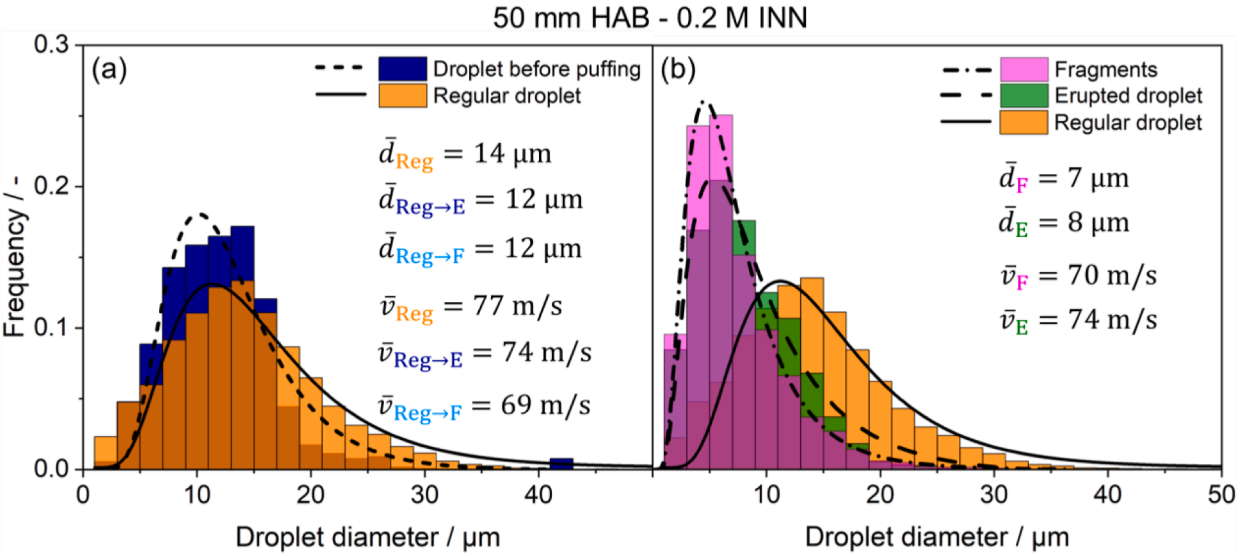

Fig. 10. Frequency histograms of (a) regular droplets and droplets before puffing and (b) regular droplets, erupted droplets, and fragments. Images acquired at 50 mm HAB and with 0.2 M INN. Also indicated are arithmetic mean diameters and mean axial velocities of droplets of the different classes.

disruption probabilities from flame-on and flame-off simulations were then averaged at each time-step for making them comparable to the experiment. Pressure was 0.98 bar, in an atmosphere of 20% O_2 and 80% N_2. The initial droplet size distribution is taken from [60] at 15 mm HAB. The distribution is discretized into 3000 weighted simulation droplets. Droplets are assumed to burn independently of each other. The total simulation time of 0.6 ms was discretized into 6000 time steps (each 10^{-7} s) with droplets starting at 15 mm HAB.

In the following, visualizations of regular, disrupting, and disrupted droplets are shown. Then, a statistical analysis of droplet disruption in SFS of iron oxide nanoparticles is provided. First, probabilities for droplet disruption are given as a function of INN concentration and HAB. Then, droplet sizes, velocities, and concentrations are shown and discussed.

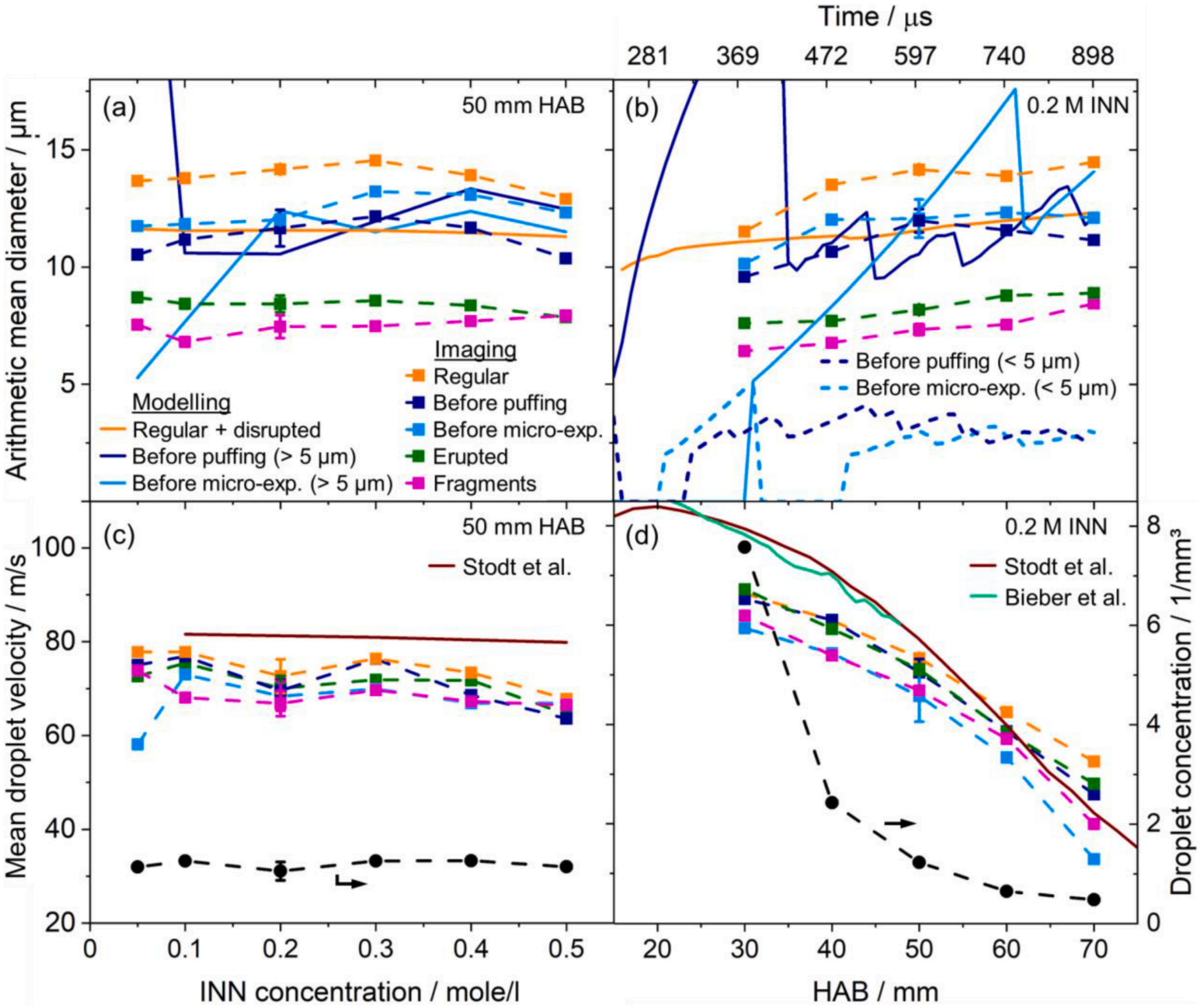

Fig. 11. (a, b) Arithmetic mean diameter and (c, d) mean velocities of regular droplets (regular + disrupted in the modelling), droplets before puffing and micro-explosion, erupted droplets, and fragments. Modelling results of droplets before disruption differentiate large and small modes. (c, d) Overall droplet concentration from imaging. The error bars at 50 mm HAB and 0.2 M INN indicate the standard deviation among three individual measurements.

3. Results and discussion

3.1. Disruption sequences

Fig. 7 shows representative sequences of regular droplets, puffing, and erupted droplets, all acquired at 50 mm HAB and with varying INN concentrations (0.1 - 0.5 M INN in EtOH/EHA). In-focus droplets have a "dark" spot in the center which results from the droplets acting as micro lenses, thus focusing the transmitted light. Sequence 3 shows a regular droplet moving substantially transverse to the focal plane and therefore becoming rapidly defocused. Sequences 4 and 5 show counterclockwise rotation of the puffing droplet while ejecting a secondary droplet, as also observed in [38]. In sequence 5, the white arrow indicates a secondary droplet, ejected at 16.8 μs, which immediately micro-explodes at 19.6 μs. Even though we define puffing as the ejection of a single secondary droplet, some images, e.g., in sequences 6 and 7, show more than one. Those were too small or too defocused for being detected so that the sequences were assigned to puffing. However, these events then still show a comparatively moderate disruption. Considering the short time droplets remain in-focus, erupted droplets, shown in sequences 8 and 9, are expected to have experienced puffing slightly upstream from the FOV.

Fig. 8 shows sequences of micro-explosions and fragments. Again, the images were acquired at 50 mm HAB and with varying INN concentrations. Nearly all micro-explosion sequences, in particular sequences 2, 4, 5, and 7 show substantial swelling of the droplet before fragmentation. This is attributed to the growth of a gas bubble within the droplet. As opposed to puffing, the bubble growth is most likely initiated in the center of the droplet, thus strongly expanding the droplet before a violent disintegration [9]. In sequence 4, the expanded droplet appears to be composed of thin liquid filaments (bright and high contrast) surrounding the droplet, and by a large gas bubble in the center (low contrast). Sequence 5 indicates a very symmetrical bubble growth and collapse towards the center of the droplet. Here, between 5.6 and 8.4 μs, the droplet diameter increases by a factor of 3.5 which increases the volume more than 40 times. This corresponds to a rate of expansion in the radius of up to 8 m/s. However, the radially ejected fragments rapidly adapt to the dominant vertical momentum of the gas flow, which is in line with the work from Stodt et al. [39] and our own previous work [40]. In single-droplet experiments of precursor-laden and emulsified droplets, the parent and secondary droplets' radial velocity component is lower [68] but more clearly visible [39]. Sequences 1, 6, and 7 show the bubble attaching either to the top (sequence 1) or bottom (sequences 6 and 7) of the droplet, indicating a decentral nucleation of the bubble. In sequence 7, this then results in jetting and the ejection of secondary droplets towards the bottom. In all sequences, the expanded droplet is visible in solely a single image. Thus, the droplet expansion and subsequent collapse happen within 5.6 μs or less.

Sequences 9 and 10 show fragments, resulting from a micro-explosion which happened slightly upstream, as with erupted droplets in Fig. 7. Interestingly and like in sequence 5 in Fig. 7, the fragment on the left in sequence 10 shows an expansion and subsequent micro-explosion between 5.6 and 11.2 μs. Also, the fragment in the top right in sequence 3 shows an elongation and micro-explosion between 8.4 and 16.8 μs. This is consistent with our previous work [40] and [36,69] and shows the quick creation of small droplets from larger parent droplets. The following section presents the probabilities for droplet disruption as well as sizes and velocities of droplets participating in disruption processes from imaging and modelling.

3.2. *Statistical analysis from imaging and modelling*

Of all sequences that contain features in-focus, Fig. 9a and b plot the relative frequencies (which can be understood as probabilities) that show regular + disrupted droplets and puffing or micro-explosion. Probabilities are shown versus the INN concentration at 30 mm HAB and versus the HAB at 0.2 M INN. The dashed lines with symbols show results from the imaging measurements and the solid lines from the modelling. On average, a coherent sequence is 4 to 5 illuminations ‘long’. This corresponds to 8.3 and 11.1 μs lifetime. Beyond these times, droplets are either defocused, have evaporated, or micro-exploded into very small fragments with sizes below the detection limit. Thus, the probabilities indicated in Fig. 9 are given per 10 μs lifetime (which corresponds to 1 mm travelled distance in the modelling). As an example, in each measurement at 50 mm HAB about 1–2% (1500-3000) of the images contain in-focus features while the rest is empty. The error bars in the experimental results at 0.2 M INN and 50 mm HAB indicate the standard deviation among three individual measurements and thus represent the repeatability of the results. The accumulated residence time of droplets in the flame as a function of HAB, indicated at the top right, was calculated with the mean droplet velocities from [59].

Imaging and modelling show a clear increase in the probability of droplet disruption with increasing INN concentration. The probability for puffing plateaus at 7.8% and 11.5% in imaging and modelling, respectively. Imaging and modelling find the probability for micro-explosion reaching 5.4% and 6.6%, respectively, at 0.5 M INN. While it also plateaus in the experiment, it is increasing in the modelling from 0.4 M onward.

Fig. 9b shows the probabilities versus the HAB and at 0.2 M INN. Imaging suggests that puffing and micro-explosion also occur further upstream than 20 mm HAB. In fact, modelling predicts puffing at already 15 mm HAB (from predominantly small droplets) while micro-explosion occurs from about 20 mm HAB onward when first superheated droplets have developed a particle shell. The ‘zig-zag’ traces in the modelling result from successive disruption of the most common droplet size in a certain time/HAB interval and the subsequent creation of many fragments, yielding rapid changes in the overall droplet concentration. In the experiment this is not observed due to averaging multiple ‘droplet swarms’ over time. In the modelling, downstream of 20 mm HAB, decomposition and particle accumulation are slow in secondary droplets. This results in a slight decrease in the micro-explosion probability between 20 and 42 mm HAB. Then, secondary droplets and large primary droplets begin to micro-explode resulting in multiple steps slightly increasing the micro-explosion probability to 4.5% at 70 mm HAB. In contrast to this, puffing tends to become much more likely with increasing HAB as droplet fragments are assumed to be superheated from the start and reaches a probability of 11.7% at 70 mm HAB. The imaging suggests that the probability for droplet disruption is highest at 30 mm HAB with about 9% and decreases towards higher HABs to 5%.

Fig. 9c and d show the probabilities for finding an erupted droplet or fragments. For both the variation in the INN concentration and in the HAB, the probabilities for finding an erupted droplet or fragments follow the ones of puffing and micro-explosion, respectively, in good agreement (with the difference being larger at 30 mm HAB). This shows that they were produced slightly upstream of the FOV and under very similar conditions. This finding is supported by the fact that disrupted droplets rapidly evaporate or become defocused (due to the undirected momentum introduced by the disruption).

Fig. 10a shows frequency histograms, extracted from imaging, of the area-equivalent diameter of regular, non-disrupting droplets, and droplets before puffing. Histograms of the diameter of erupted droplets and fragments are shown in Fig. 10b. Also indicated are arithmetic mean diameters and mean velocities of the different droplet classes. The results are from 750 000 images, acquired at 0.2 M INN and 50 mm HAB, which yield diameters of 45 404 in-focus droplets. All distributions follow log-normal distributions in good agreement. Droplets before puffing and micro-explosion (histogram not shown for the latter) are on average 15% smaller and 5 to11% slower than non-disrupting droplets. The longer residence time in the flame of droplets before disruption explains that they are smaller than non-disrupting ones and that they had sufficient time to superheat and/or build up a “sufficiently” viscous shell.

Erupted droplets and fragments are about 45% smaller than regular, non-disrupting droplets, as shown in Fig. 10b. This increases the droplets’ specific surface area on average by a factor of two. Consistent with droplets before disruption, erupted droplets and fragments are slower than regular droplets.

Fig. 11a and b show the arithmetic mean diameters of regular droplets (regular + disrupted in the modelling), disrupting, and disrupted droplets versus (a) the INN concentration at 50 mm HAB and versus (b) the HAB at 0.2 M INN. Diameters of droplets before puffing and micro-explosion in the modelling indicate a highly bimodal distribution so that they were averaged among two different intervals. The small mode covers all droplets before disruption with diameters < 5 μm and the large mode those with diameters > 5 μm which is comparable with the imaging. This is because the imaging does not find any disruptions for droplets smaller than 5 μm. On the one hand, it is possible that ejected secondary droplets are too small for being detected. On the other hand, this might also result from substantial increase in the liquid’s static pressure of very small droplets (Young-Laplace equation), thus inhibiting bubble nucleation. For better visibility, Fig. 11a shows only the large mode from the modelling while Fig. 11b shows large and small mode.

In Fig. 11a, imaging finds the droplet diameters mostly independent of the INN concentration, yielding an overall arithmetic mean diameter (weighted average among all droplet classes) of 13.3 μm (Stodt et al. found an arithmetic mean diameter of 16 μm between 0.1–0.5 M INN and under the same conditions [60]). The modelling predicts the diameter of regular and disrupted droplets approximately constant at 11.3 μm. In the imaging, increasing the INN concentration from 0.05 to 0.3 M INN increases the mean size of droplets before puffing and micro-explosion by 14%. Up to 0.2 M INN, this is qualitatively consistent with the modelling of droplets before micro-explosion where the sharp increase in the mean diameter results from an earlier particle-shell formation in all droplets. The produced fragments rapidly superheat and decrease the mean diameter of droplets before puffing in the modelling from 34 μm at 0.05 M INN to on average 12 μm between 0.1 and 0.5 M INN. Imaging and modelling show a decrease in the size of droplets before disruption beyond 0.3-0.4 M INN. This occurs due to small already disrupted droplets undergoing puffing and micro-explosion again. Over the entire concentration range, imaging finds disrupted droplets and droplets before disruption 43 and 15%, respectively, smaller than regular droplets.

Fig. 11b shows the evolution of mean diameters versus the HAB and at an INN concentration of 0.2 M INN. Imaging finds the overall arithmetic mean diameter increasing from 10.5 to 13.3 μm between 30 and 70 mm HAB, respectively. Under the same conditions but with 0.1 M INN, Stodt et al. found mean diameters of 10 μm and 16 μm at 30 and 70 mm HAB, respectively [60]. The following discussion on the modelling results first considers the large mode of droplets before disruption. Droplets before puffing increase in size until 34 mm HAB (not visible). After the onset of micro-explosion at 21 mm HAB, fragments rapidly superheat and undergo puffing, decreasing the diameter of droplets before puffing which eventually oscillates around 11 μm until 70 mm HAB. The diameter of droplets before micro-explosion increases with the HAB, as also larger size classes tend to form a particle shell with increasing residence time in the flame. At 61 mm HAB, fragments micro-explode again which causes the sharp drop in the diameter of droplets before micro-explosion. The small modes of droplets before puffing and micro-explosion first decrease and vanish when the corresponding large modes evolve. Then the small modes of droplets before puffing and micro-explosion increase again due to superheating and shell formation in fragments and eventually become 3.1 μm and 2.7 μm, respectively.

Fig. 11c and d show the mean droplet velocity and concentration from imaging and as functions of the INN concentration (c) and the HAB (d). Consistent with Stodt et al. [60], the droplet velocity in Fig. 11c is approximately constant but very slightly decreasing with the INN concentration for all droplet classes. At all INN concentrations, regular droplets are faster than disrupting and disrupted droplets. The outlier at 0.05 M INN results from averaging only eight velocities of droplets before micro-explosion. The droplet concentration is about 1.2 droplets/mm^3 at all INN concentrations. Fig. 11d shows the velocities of all droplet classes decreasing with increasing HAB. With PDI, Bieber et al. and Stodt et al. [59,60] found droplet velocities higher than the imaging at low HABs and matching the imaging at higher HABs. Most likely, very small droplets, following the gas flow, and not caught by the imaging cause the difference between PDI and imaging. Over the entire HAB range, droplets before micro-explosion and fragments are slower, at 70 mm HAB even 37% and 24%, respectively, than regular droplets. Between 50 and 70 mm HAB, also droplets before puffing and erupted droplets are slower than regular droplets. The velocities of erupted droplets and fragments follow the ones of droplets before puffing and micro-explosion, respectively, in very good agreement. This indicates that disruption does not significantly accelerate disrupted droplets. The droplet concentration decreases from almost 7.5 droplets/mm^3 at 30 mm HAB to 0.5 droplets/mm^3 at 70 mm HAB.

4. Conclusions

Thermally-induced secondary atomization, i.e., droplet disruption, of precursor-laden droplets in spray-flame synthesis (SFS) was investigated with high-speed imaging and population balance modelling. Droplets were visualized in SFS with shadowgraphy in high spatiotemporal resolution. Image analysis was developed to extract probabilities for puffing and micro-explosion as well as sizes, velocities, and concentrations of regular, disrupting, and disrupted droplets. For comparison, population balance modelling of droplet evaporation, superheating, and breakup was performed. The liquid consisted of 35% ethanol (EtOH) and 65% 2-ethylhexanoic acid (EHA) as solvent and variable amounts of iron(III) nitrate nonahydrate (INN) were added. The model predicts that chemical reaction and decomposition of the precursor within the liquid lead to precipitation of iron hydroxide particles, being responsible for droplet disruption. Imaging and modelling of droplet disruption were done for INN concentrations in the range of 0.05 to 0.5 M and heights above the burner (HAB) between 20 and 70 mm.

Images of micro-explosions mostly show a substantial expansion of the droplet, attributed to bubble growth, before a violent disintegration. Micro-explosion occurs very fast, i.e., expansion and fragmentation within about 5 μs, while puffing is comparatively slow. Visualizations of disruptions sometimes show a second disruption immediately after the first one.

Imaging and modelling find a significant increase in the disruption probability with the INN concentration. In the experiment, probabilities for puffing and micro-explosion reach 8% and 5% per 10 μs, respectively, at 0.5 M INN. Modelling finds probabilities for puffing and micro-explosion of 12 and 7%, respectively, at 0.5 M INN. Imaging finds the disruption probability of about 7% being mostly independent of the HAB while the modelling, in particular for puffing, finds it increasing with the HAB. Since disruptions of very small droplets (smaller than about 5 μm) are rarely found in the experiment but account for a substantial fraction in the modelling, modelled probabilities are substantially higher. Lacking small disrupting droplets in the imaging partially comes from not detecting droplets smaller than 2 μm. On the other hand, it might also result from the increase in the liquid's static pressure of very small droplets (Young-Laplace equation) and thus inhibit bubble nucleation. However, the probabilities from imaging and modelling suggest that between 20 and 70 mm HAB (about 600 μs) a droplet will experience disruption multiple times. The quantitative agreement of the disruption probabilities from modelling and imaging suggests that precursor decomposition and particle precipitation are a plausible cause for droplet disruption in metal-nitrate-laden droplets.

Independent of the INN concentration and the HAB, the experiment finds droplets before puffing and micro-explosion being 15% smaller than regular, non-disrupting droplets. Already disrupted droplets have a 45% smaller mean diameter than regular droplets indicating their strong impact in increasing the liquid's specific surface area. Mean diameters of all droplet classes are largely independent of the INN concentration in imaging and modelling. In the experiment, mean diameters increase by about 25% between 30 and 70 mm HAB. Along the same height, the droplet concentration decreases from 7.5 to 0.5 droplets/mm^3. Disrupting and disrupted droplets are, particularly at higher HAB, slower than regular droplets. The velocities of disrupted droplets are similar to those of their corresponding parent droplets, indicating that disruption does not accelerate ejected secondary droplets.

Declaration of Competing Interest

The authors declare that they have no known competing financial interests or personal relationships that could have appeared to influence the work reported in this paper.

Data availability

Data will be made available on request.

Acknowledgments

This work was supported by the German Research Foundation (DFG) within the Priority Program SPP 1980 SpraySyn under project numbers 447500013 and 375857056. The DFG Mercator Fellowship held by Greg Smallwood is supported by project number 374957702.

Appendix

A1 Calculation of the droplet concentration

The droplet concentration c is calculated as follows:

$$c = \frac{N}{(w_{\mathrm{FOV}}\cdot h_{\mathrm{FOV}}\cdot d_{\mathrm{FOV}})\cdot\frac{h_{\mathrm{FOV}}+\bar{v}_{\mathrm{d}}\cdot t_{\mathrm{LED}}\cdot 2}{h_{\mathrm{FOV}}}\cdot 150\ 000}$$

Here, N is the total number of in-focus features in a measurement (150 000 images). w_{FOV}, h_{FOV}, and d_{FOV} are the width, height, and depth of the measurement volume, respectively, resulting to 0.039 mm^3. The second factor in the denominator accounts for the increase in the height of the measurement volume due to the downstream flow, where $\bar{v}_{\mathrm{d}}$ is the average droplet velocity at the corresponding HAB and t_{LED} the time between two LED pulses. The corrected measurement volume (product of first and second factors in the denominator) is then multiplied with the number of images in the measurement.

A2 Velocity-based extraction of illuminations

Due to the strong vertical component of the droplet velocity, features illuminated multiple times are found within small horizontal distance (maximum 50 columns from the horizontally central feature; value found by visual inspection). If in this group also the distance from the bottommost to the topmost feature, h_{group}, is less than 360 rows (640 µm), those features/droplets stem from one, two, or three illuminations and are considered a group. 360 rows correspond to the distance that about 95% of the droplets at 30 mm HAB (height where droplets are fastest among the heights where automatic image analysis was applied) travel during three LED illuminations (5.56 µs). Fig. 5 on the left shows a segmented image of features that fulfill these two conditions.

Then, each feature is assigned to an illumination within a group, as shown in Fig. 5 and described in the following. First, the number of illuminations in a group is determined by taking into account h_{group}, the average droplet velocity $\bar{v}_{\mathrm{d}}$ at the corresponding HAB, the velocity's standard deviation $\sigma_{v_{\mathrm{d}}} = 0.15\cdot\bar{v}_{\mathrm{d}}$ ($\bar{v}_{\mathrm{d}}$ and $\sigma_{v_{\mathrm{d}}}$ from [59]), and the time between two LED pulses $t_{\mathrm{LED}} \approx 2.78\ \mu s$. The velocity follows a normal distribution. Thus, $(\bar{v}_{\mathrm{d}} - 4\cdot\sigma_{v_{\mathrm{d}}})\cdot t_{\mathrm{LED}}$ is the distance which is at least travelled by almost 100% of the droplets within t_{LED}. For example, at 50 mm HAB $\bar{v}_{\mathrm{d}}$ is 78 m/s and $\sigma_{v_{\mathrm{d}}}$ 11.7 m/s such that this lower boundary becomes 50 pixels. Feature groups with h_{group} shorter than 50 pixels then show a single illumination. At the same time, $(\bar{v}_{\mathrm{d}} + 2\cdot\sigma_{v_{\mathrm{d}}})\cdot t_{\mathrm{LED}}$ denotes the distance which is maximally travelled by 97.7% of the droplets within t_{LED} and becomes 160 pixels at 50 mm HAB. Thus, groups with h_{group} longer 50 pixels and shorter than 160 pixels show features from two illuminations and groups with h_{group} longer than 160 pixels show features from three illuminations. Table 1 summarizes this classification.

Table 1
Bounding box height intervals for determination of no. of illuminations in a group

Case 1	$h_{\mathrm{group}} < (\bar{v}_{\mathrm{d}} - 4\cdot\sigma_{v_{\mathrm{d}}})\cdot t_{\mathrm{LED}}$	Single illumination
Case 2	$(\bar{v}_{\mathrm{d}} - 4\cdot\sigma_{v_{\mathrm{d}}})\cdot t_{\mathrm{LED}} < h_{\mathrm{group}} < (\bar{v}_{\mathrm{d}} + 2\cdot\sigma_{v_{\mathrm{d}}})\cdot t_{\mathrm{LED}}$	Two illuminations
Case 3	$(\bar{v}_{\mathrm{d}} + 2\cdot\sigma_{v_{\mathrm{d}}})\cdot t_{\mathrm{LED}} < h_{\mathrm{group}}$	Three illuminations

In all visually inspected images, features from a single illumination cover less than 50 pixels vertical distance such that 100% of the groups showing a single illumination are correctly identified. 97.7% of the features illuminated two times are correctly found. The fastest 2.3% are erroneously assigned to three illuminations, while conversely the slowest 1.6% of the features illuminated three times are erroneously assigned to two illuminations.

Once all droplets are assigned to a group and each droplet is assigned to an illumination within that group, the velocity between two consecutive illuminations is calculated. First, the projected distance l in the x-y-plane is calculated by $l = \sqrt{(x_2^2 - x_1^2) + (y_2^2 - y_1^2)}$. Here, $(x_1|y_1)$ and $(x_2|y_2)$ are the center coordinates of the bounding boxes, the smallest rectangle enclosing all features of an illumination, of the first and second illumination, respectively. The velocity then results from the division by the time between two LED pulses $t_{\mathrm{LED}} = 2.78\ \mu s$ to $v = \frac{l}{t_{\mathrm{LED}}}$. The z-component of the velocity vector, the one perpendicular to the image plane, is not considered due to the line-of-sight measurement such that the calculated velocities represent projections into the x-y-plane. However, droplets with significant velocity components in the z-direction would rapidly become defocused, and thereby rejected in image analysis.

References

[1] Mädler L, Kammler HK, Mueller R, Pratsinis SE. Controlled synthesis of nanostructured particles by flame spray pyrolysis. J Aerosol Sci 2002;33(2): 369–89. https://doi.org/10.1016/S0021-8502(01)00159-8.

[2] Schneider F, Suleiman S, Menser J, Borukhovich E, Wlokas I, Kempf A, et al. SpraySyn—A standardized burner configuration for nanoparticle synthesis in spray flames. Rev Sci Instrum 2019;90(8):085108. https://doi.org/10.1063/1.5090232.

[3] Meierhofer F, Fritsching U. Synthesis of metal oxide nanoparticles in flame sprays: review on process technology, modeling, and diagnostics. Energy Fuels 2021;35 (622). https://doi.org/10.1021/acs.energyfuels.0c04054.

[4] Strobel R, Pratsinis S. Effect of solvent composition on oxide morphology during flame spray pyrolysis of metal nitrates. Phys Chem Chem Phys 2011;13:9246–52. https://doi.org/10.1039/c0cp01416h.

[5] Rosebrock CD, Riefler N, Wriedt T, Mädler L, Tse SD. Disruptive burning of precursor/solvent droplets in flame-spray synthesis of nanoparticles. AIChE J 2013; 59(12):4553–66. https://doi.org/10.1002/aic.14234.

[6] Rosebrock CD, Wriedt T, Mädler L, Wegner K. The role of microexplosions in flame spray synthesis for homogeneous nanopowders from low-cost metal precursors. AIChE J 2016;62(2):381–91. https://doi.org/10.1002/aic.15056.

[7] Witte A, Mädler L. Single droplet combustion of iron nitrate-based precursor solutions: Investigation of time- and size scales of isolated burning FSP-droplets. Appl. Energy Combust. Sci. 2023;14:100147. https://doi.org/10.1016/j.jaecs.2023.100147.

[8] Basu S, Miglani A. Combustion and heat transfer characteristics of nanofluid fuel droplets: a short review. Int J Heat Mass Transf 2016;96:482–503. https://doi.org/10.1016/j.ijheatmasstransfer.2016.01.053.

[9] Shinjo J, Xia J, Ganippa LC, Megaritis A. Physics of puffing and microexplosion of emulsion fuel droplets. Phys Fluids 2014;26(10):103302. https://doi.org/10.1063/1.4897918.

[10] Stodt M, Liu C, Li S, Mädler L, Fritsching U, Kiefer J. Phase-selective laser–induced breakdown spectroscopy in flame spray pyrolysis for iron oxide nanoparticle synthesis. Proc Combust Inst 2021;38(1):1711–8. https://doi.org/10.1016/j.proci.2020.06.092.

[11] Angel S, Neises J, Dreyer M, Friedel-Ortega K, Behrens M, Wang Y, et al. Spray-flame synthesis of La(Fe, Co)O3 nano-perovskites from metal nitrates. AIChE J 2019;66(1). https://doi.org/10.1002/aic.16748.

[12] Avedisian CT, Andres RP. Bubble nucleation in superheated liquid—liquid emulsions. J Colloid Interface Sci 1978;64(3):438–53. https://doi.org/10.1016/0021-9797(78)90386-7.

[13] Lasheras J, Fernandez-Pello A, Dryer F. Initial observations on the free droplet combustion characteristics of water-in-fuel emulsions. Combust Sci Technol 1979; 21(1-2):1–14. https://doi.org/10.1080/00102207908946913.

[14] Law CK, Lee CH, Srinivasan N. Combustion characteristics of water-in-oil emulsion droplets. Combust Flame 1980;37:125–43. https://doi.org/10.1016/0010-2180(80)90080-2.

[15] Mura E, Josset C, Loubar K, Huchet G, Bellettre J. Effect of dispersed water droplet size in microexplosion phenomenon for water in oil emulsion. At Sprays 2010;20: 791–9. https://doi.org/10.1615/AtomizSpr.v20.i9.40.

[16] Suzuki Y, Harada T, Watanabe H, Shoji M, Matsushita Y, Aoki H, et al. Visualization of aggregation process of dispersed water droplets and the effect of aggregation on secondary atomization of emulsified fuel droplets. Proc Combust Inst 2011;33(2):2063–70. https://doi.org/10.1016/j.proci.2010.05.115.

[17] Califano V, Calabria R, Massoli P. Experimental evaluation of the effect of emulsion stability on micro-explosion phenomena for water-in-oil emulsions. Fuel 2014;117: 87–94. https://doi.org/10.1016/j.fuel.2013.08.073.

[18] Rao DCK, Karmakar S, Basu S. Bubble dynamics and atomization mechanisms in burning multi-component droplets. Phys Fluids 2018;30(6):067101. https://doi.org/10.1063/1.5035384.

[19] Zhang X, Li T, Wang B, Wei Y. Superheat limit and micro-explosion in droplets of hydrous ethanol-diesel emulsions at atmospheric pressure and diesel-like conditions. Energy 2018;154:535–43. https://doi.org/10.1016/j.energy.2018.04.176.

[20] Sazhin SS, Rybdylova O, Crua C, Heikal M, Ismael MA, Nissar Z, et al. A simple model for puffing/micro-explosions in water-fuel emulsion droplets. Int J Heat Mass Transf 2019;131:815–21. https://doi.org/10.1016/j.ijheatmasstransfer.2018.11.065.

[21] Sazhin SS, Bar-Kohany T, Nissar Z, Antonov D, Strizhak PA, Rybdylova OD. A new approach to modelling micro-explosions in composite droplets. Int J Heat Mass Transf 2020;161:120238. https://doi.org/10.1016/j.ijheatmasstransfer.2020.120238.

[22] Antonov DV, Fedorenko RM, Strizhak PA, Nissar Z, Sazhin SS. Puffing/micro-explosion in composite fuel/water droplets heated in flames. Combust Flame 2021; 233:111599. https://doi.org/10.1016/j.combustflame.2021.111599.

[23] Lasheras JC, Yap LT, Dryer FL. Effect of the ambient pressure on the explosive burning of emulsified and multicomponent fuel droplets. Symp Combust Proc 1985;20(1):1761–72. https://doi.org/10.1016/S0082-0784(85)80673-1.

[24] Lasheras JC, Fernandez-Pello AC, Dryer FL. On the disruptive burning of free droplets of alcohol/n-paraffin solutions and emulsions. Symp Combust Proc 1981; 18(1):293–305. https://doi.org/10.1016/S0082-0784(81)80035-5.

[25] Wang CH, Liu XQ, Law CK. Combustion and microexplosion of freely falling multicomponent droplets. Combust Flame 1984;56(2):175–97. https://doi.org/10.1016/0010-2180(84)90036-1.

[26] Mikami M, Kojima N. An experimental and modeling study on stochastic aspects of microexplosion of binary-fuel droplets. Proc Combust Inst 2002;29(1):551–9. https://doi.org/10.1016/S1540-7489(02)80071-2.

[27] Wood BJ, Wise H, Inami SH. Heterogeneous combustion of multicomponent fuels. Combust Flame 1960;4:235–42. https://doi.org/10.1016/S0010-2180(60)80027-2.

[28] Shen S, Sun K, Che Z, Wang T, Jia M. Puffing and micro-explosion of heated droplets for homogeneous ethanol-propanol-hexadecane fuel and micro-emulsified ethanol-biodiesel-hexadecane fuel. Appl Therm Eng 2020;165:114537. https://doi.org/10.1016/j.applthermaleng.2019.114537.

[29] Antonov DV, Fedorenko RM, Kuznetsov GV, Strizhak PA. Modeling the micro-explosion of miscible and immiscible liquid droplets. Acta Astronaut 2020;171: 69–82. https://doi.org/10.1016/j.actaastro.2020.02.040.

[30] Kumar A, Chen HW, Yang S. Modeling microexplosion mechanism in droplet combustion: puffing and droplet breakup. Energy 2023;266:126369. https://doi.org/10.1016/j.energy.2022.126369.

[31] Kumar A, Chen HW, Yang S. Diffusion and its effects on soot production in the combustion of emulsified and nonemulsified fuel droplets. Energy 2023;267: 126521. https://doi.org/10.1016/j.energy.2022.126521.

[32] Wornat MJ, Porter BG, Yang NYC. Single droplet combustion of biomass pyrolysis oils. Energy Fuels 1994;8(5):1131–42. https://doi.org/10.1021/ef00047a018.

[33] Mizutani Y, Muraoka M. *In situ* observation of microexplosion of emulsion droplets in spray flames. At Sprays 2001;11(5):12. https://doi.org/10.1615/AtomizSpr.v11.i5.30.

[34] Fuchihata M, Shuko T, Ida T. Observation of microexplosion in light oil-water emulsion spray flame. Trans Jpn Soc Mech Eng B 2003;69(682):1503–8. https://doi.org/10.1299/kikaib.69.1503.

[35] Watanabe H, Okazaki K. Visualization of secondary atomization in emulsified-fuel spray flow by shadow imaging. Proc Combust Inst 2013;34(1):1651–8. https://doi.org/10.1016/j.proci.2012.07.005.

[36] Watanabe H, Shoji Y, Yamagaki T, Hayashi J, Akamatsu F, Okazaki K. Observation of droplet behavior of emulsified fuel in secondary atomization in flame. J Therm Sci Technol 2014;9(2). https://doi.org/10.1299/jtst.2014jtst0009.

[37] Ismael M, Heikal MR, Aziz AAR, Crua C, El Adawy M, Nissar Z, et al. Investigation of puffing and micro-explosion of water-in-diesel emulsion spray using shadow imaging. Energies 2018;11(9):2281. https://doi.org/10.3390/en11092281.

[38] Stodt, M.F.B., Groeneveld, J.D., Mädler, L., Kiefer, J., Fritsching, U., Combustion of multi-component drops during flame spray pyrolysis, in Proceedings of the 15th international conference on liquid atomization and spray systems (ICLASS), August 30th – September 2nd 2021, Edinburgh, UK.

[39] Stodt M, Groeneveld J, Mädler L, Kiefer J, Fritsching U. Microexplosions of multicomponent drops in spray flames. Combust Flame 2022;240(6):112043. https://doi.org/10.1016/j.combustflame.2022.112043.

[40] Jüngst N, Smallwood GJ, Kaiser SA. Visualization and image analysis of droplet puffing and micro-explosion in spray-flame synthesis of iron oxide nanoparticles. Exp Fluids 2022;63(3):60. https://doi.org/10.1007/s00348-022-03411-y.

[41] Stodt MFB, Gonchikzhapov M, Kasper T, Fritsching U, Kiefer J. Chemistry of iron nitrate-based precursor solutions for spray-flame synthesis. Phys Chem Chem Phys 2019;21(44):24793–801. https://doi.org/10.1039/C9CP05007H.

[42] Kunstmann B, Kohns M, Hasse H. Thermophysical Properties of Mixtures of 2-Ethylhexanoic Acid and Ethanol. J Chem Eng Data 2023;68(2):330–8. https://doi.org/10.1021/acs.jced.2c00689.

[43] Rosebrock, C.D., On the disruptive combustion of single metal-organic precursor solution droplets. Dissertation, Bremen: University of Bremen, 2017.

[44] Li, H., Flame spray pyrolysis for synthesizing functional nanoparticles: Fundamental investigations on single and double droplet combustion. Dissertation, Bremen: University of Bremen, 2021.

[45] Cochran EA, Park DH, Kast MG, Enman LJ, Perkins CK, Mansergh RH, et al. Role of combustion chemistry in low-temperature deposition of metal oxide thin films from solution. Chem Mater 2017;29(21):9480–8. https://doi.org/10.1021/acs.chemmater.7b03618.

[46] Salvatore DA, Dettelbach KE, Hudkins JR, Berlinguette CP. Near-infrared driven decomposition of metal precursors yields amorphous electrocatalytic films. Sci Adv 2015;1(2):e1400215. https://doi.org/10.1126/sciadv.1400215.

[47] Dettelbach KE, Salvatore DA, Bottomley A, Berlinguette CP. Tracking precursor degradation during the photo-induced formation of amorphous metal oxide films. J Mater Chem A 2018;6(10):4544–9. https://doi.org/10.1039/C7TA10369G.

[48] Tischendorf R, Simmler M, Weinberger C, Bieber M, Reddemann M, Fröde F, et al. Examination of the evolution of iron oxide nanoparticles in flame spray pyrolysis by tailored *in situ* particle sampling techniques. J Aerosol Sci 2021;154:105722. https://doi.org/10.1016/j.jaerosci.2020.105722.

[49] Mosadegh S, Ghaffarkhah A, van der Kuur C, Arjmand M, Kheirkhah S. Graphene oxide doped ethanol droplet combustion: Ignition delay and contribution of atomization to burning rate. Combust Flame 2022;238:111748. https://doi.org/10.1016/j.combustflame.2021.111748.

[50] Gan Y, Qiao L. Combustion characteristics of fuel droplets with addition of nano and micron-sized aluminum particles. Combust Flame 2011;158(2):354–68. https://doi.org/10.1016/j.combustflame.2010.09.005.

[51] Pandey K, Basu S. High vapour pressure nanofuel droplet combustion and heat transfer: Insights into droplet burning time scale, secondary atomisation and coupling of droplet deformations and heat release. Combust Flame 2019;209(2): 167–79. https://doi.org/10.1016/j.combustflame.2019.07.043.

[52] Dai M, Wang J, Wei N, Wang X, Xu C. Experimental study on evaporation characteristics of diesel/cerium oxide nanofluid fuel droplets. Fuel 2019;254: 115633. https://doi.org/10.1016/j.fuel.2019.115633.

[53] Wang J, Qiao X, Ju D, Wang L, Sun C. Experimental study on the evaporation and micro-explosion characteristics of nanofuel droplet at dilute concentrations. Energy 2019;183:149–59. https://doi.org/10.1016/j.energy.2019.06.136.

[54] Jang GM, Kim NI. Investigation on breakup characteristics of multicomponent single droplets of nanofluid and water-in-oil emulsion using a pulse laser. Fuel 2022;310:122300. https://doi.org/10.1016/j.fuel.2021.122300.

[55] Miglani A, Basu S. Coupled mechanisms of precipitation and atomization in burning nanofluid fuel droplets. Sci Rep 2015;5:15008. https://doi.org/10.1038/srep15008.

[56] Ojha PK, Maji R, Karmakar S. Effect of crystallinity on droplet regression and disruptive burning characteristics of nanofuel droplets containing amorphous and crystalline boron nanoparticles. Combust Flame 2018;188:412–27. https://doi.org/10.1016/j.combustflame.2017.10.005.

[57] Mosadegh S, Kheirkhah S. The role of atomization in the coupling between doped droplets dynamics and their flames. Phys Fluids 2022;34:087109. https://doi.org/10.1063/5.0098175.

[58] Skenderović I, Jüngst N, Kaiser SA, Kruis FE. A Population balance method for simulation of particle-induced droplet breakup in spray flame synthesis and suspension spray combustion. Appl Energy Combust Sci 2023. https://doi.org/10.1016/j.jaecs.2023.100162. In press.

[59] Bieber M, Al-Khatib M, Fröde F, Pitsch H, Reddemann M, Schmid HJ, et al. Influence of angled dispersion gas on coaxial atomization, spray and flame formation in the context of spray-flame synthesis of nanoparticles. Exp Fluids 2021; 62(5). https://doi.org/10.1007/s00348-021-03196-6.

[60] Stodt MFB, Kiefer J, Fritsching U. Drop dynamics in heterogeneous spray flames for nanoparticle synthesis. At Sprays 2020;30(11):779–97. https://doi.org/10.1615/AtomizSpr.2020034819.

[61] Otsu N. A threshold selection method from gray-level histograms. IEEE Trans Syst Man Cybern 1979;9(1):62–6. https://doi.org/10.1109/TSMC.1979.4310076.

[62] Law CK. Internal boiling and superheating in vaporizing multicomponent droplets. AIChE J 1978;24(4):626–32. https://doi.org/10.1002/aic.690240410.

[63] Prakash A, Bapat AP, Zachariah MR. A simple numerical algorithm and software for solution of nucleation, surface growth, and coagulation problems. Aerosol Sci Technol 2003;37(11):892–8. https://doi.org/10.1080/02786820300933.

[64] Mv S. Versuch einer mathematischen theorie der koagulationskinetik kolloider lösungen. Z Phys Chem 1918;92(1):129–68. https://doi.org/10.1515/zpch-1918-9209.

[65] Honig EP, Roebersen GJ, Wiersema PH. Effect of hydrodynamic interaction on the coagulation rate of hydrophobic colloids. J Colloid Interface Sci 1971;36(1): 97–109. https://doi.org/10.1016/0021-9797(71)90245-1.

[66] Keller A, Wlokas I, Kohns M, Hasse H. Solid-liquid equilibria in mixtures of iron(III) nitrate nonahydrate and ethanol or 1-propanol. Fluid Phase Equilib 2021;536: 112987. https://doi.org/10.1016/j.fluid.2021.112987.

[67] Mädler L, Lall AA, Friedlander SK. One-step aerosol synthesis of nanoparticle agglomerate films: simulation of film porosity and thickness. Nanotechnology 2006;17(19):4783. https://doi.org/10.1088/0957-4484/17/19/001.

[68] Strizhak P, Volkov R, Moussa O, Tarlet D, Bellettre J. Child droplets from micro-explosion of emulsion and immiscible two-component droplets. Int J Heat Mass Transf 2021;169:120931. https://doi.org/10.1016/j.ijheatmasstransfer.2021.120931.

[69] Antonov, D., Strizhak, P., Sazhin, S., Cascade puffing and micro-explosion in composite droplets, in Proceedings of the 3rd international conference on fluid flow and thermal science (ICFFTS`22), October 27th – 29th 2022, Seoul, South Korea.